crystals

MDPI

Article

Structural and Improper Ferroelectric Properties of $TbInO_3$ Single Crystal Grown by Laser Floating Zone

Chang Min [1,†], You Wu [1,†], Yanbin Li [1,*], Chunming Zhou [1], Sang-Wook Cheong [2], Xiaosong Lu [1], Tianyuan Zhou [1] and Le Zhang [1,*]

[1] Jiangsu Key Laboratory of Advanced Laser Materials and Devices, School of Physics and Electronics Engineering, Jiangsu Normal University, Xuzhou 221116, China
[2] Rutgers Center for Emergent Materials, Department of Physics and Astronomy, Rutgers University, Piscataway, NJ 08854, USA
* Correspondence: lyb@jsnu.edu.cn (Y.L.); njutzl@163.com (L.Z.)
† These authors contributed equally to this work.

Abstract: The honeycomb $TbInO_3$ has attracted wide research attention due to its fascinating physical properties. However, $TbInO_3$ single crystal was difficult to grow owing to the high melting point and serious volatilization of indium during the crystal growth. In this study, the volatilization of the indium element was effectively suppressed by controlling the growth atmosphere and pressure. The excess ratio of indium oxide was determined, and pure hexagonal $TbInO_3$ crystal was obtained by the laser floating zone method. Systematic studies on the crystal structure and optical and ferroelectric properties were carried out. The structure distortion resulted in the improper geometric ferroelectric revealed by single crystal diffraction and Raman spectrum measurements. The topological vortex domains and P-E hysteresis loop demonstrated the presence of ferroelectricity. $TbInO_3$ crystal has great potential application in vortex memory.

Keywords: crystal growth; ferroelectricity; topological vortex

check for updates

Citation: Min, C.; Wu, Y.; Li, Y.; Zhou, C.; Cheong, S.-W.; Lu, X.; Zhou, T.; Zhang, L. Structural and Improper Ferroelectric Properties of $TbInO_3$ Single Crystal Grown by Laser Floating Zone. *Crystals* **2023**, *13*, 287. https://doi.org/10.3390/cryst13020287

Academic Editor: Dmitry Roshchupkin

Received: 6 January 2023
Revised: 4 February 2023
Accepted: 6 February 2023
Published: 8 February 2023

Copyright: © 2023 by the authors. Licensee MDPI, Basel, Switzerland. This article is an open access article distributed under the terms and conditions of the Creative Commons Attribution (CC BY) license (https://creativecommons.org/licenses/by/4.0/).

1. Introduction

The ABO_3-type compounds, referred to as perovskites, always possess fascinating physical properties [1–10]. The structure of ABO_3 perovskites, depending on the relative radii of A- and B-cations, can be distinguished by the Goldschmidt's tolerance factor (t) given by $(rA + rO)/\sqrt{2}(rB + rO)$ [11]. An ideal perovskite is formed when $t = 1$. Many more complex structural families are derived from the cubic ABO_3 perovskite. It has been reported that ABO_3 formed in a low symmetric hexagonal structure in the narrow window of $0.83 \leq t \leq 0.85$ [12–17]. This hexagonal structure provides a fancy platform for the lattice, charge, orbital, and spin. Among them, hexagonal $R MnO_3$ (R: rare-earth) families have been widely studied owing to the intriguing magnetoelectric effect [18–22]. Compared with conventional multiferroic materials, the improper geometric ferroelectric mechanism that breaks inversion symmetry allows for the production of a two-dimensional triangular lattice of spins, which supports strong magnetoelectric coupling [23,24]. Hexagonal $R InO_3$, isostructural with $R MnO_3$, has also evoked a lot of interest in recent years owing to the coexistence of magnetism and improper geometric ferroelectricity [25–31]. Tohei et al. have predicted the existence of ferroelectricity in hexagonal $GdInO_3$ and $DyInO_3$ by first-principles calculations [32]. Tyagi et al. reported the compositional and structural tuning of electrical behavior in mixed rare earth indates [12,33,34]. The influence of the synthesis route and heat treatment on the crystal structure was also revealed [35]. Recently, we clarified the controversy of $GdInO_3$ ferroelectricity between single crystal and polycrystalline [33,36]. The structural, magnetic and ferroelectric properties in $GdInO_3$ and $EuInO_3$ crystals were investigated [36,37].

In particular, $TbInO_3$ is a quantum spin liquid candidate with a quasi-two-dimensional triangular spin-lattice, which is important for quantum computation applications [2,16,17]. Known quantum spin liquid candidate compounds are typically based on geometrically frustrated magnetic lattices, such as the kagome and triangular lattices [38]. The so-called centered honeycomb lattice structure of $TbInO_3$ determines its fascinating properties. However, the Crystallographic Information File (CIF) of $TbInO_3$ could not be found in Inorganic Crystal Structure Database (ICSD-for-WWW) or Crystallography Open Database (COD). Although the $TbInO_3$ crystals have been obtained in previous studies [2,16,17], the crystallinity of that crystal looks not good from the photograph of the cleaved surface [2], and $TbInO_3$ single crystal growth atmosphere, pressure, and the excess ratio of indium oxide is need to be optimized owing to the serious volatilization of indium at high temperature. Moreover, systematic studies on the crystal structure have not yet been carried out due to the lack of fabricated good single-crystal samples.

In the present work, pure phase $TbInO_3$ single crystal was grown by the laser floating zone method. The optimal growth atmosphere, pressure and excess ratio of indium oxide were determined. The $TbInO_3$ crystal structure was resolved, and lattice dynamics were well investigated. The optical and improper ferroelectric properties of $TbInO_3$ crystal were studied. Besides, interesting topological vortex domains were discovered.

2. Experimental

2.1. Single Crystal Growth

Tb_4O_7 and In_2O_3 with 4N purity were used as raw materials for crystal growth. They were calcined at 500 °C for 4 h to eliminate the moisture and adsorbed gases. Tb_4O_7 and In_2O_3 were weighted by stoichiometric ratio, and excess In_2O_3 was added to compensate for the volatilization of indium during crystal growth. The ingredients were mixed well in a mortar and compressed into pellets. Pure $TbInO_3$ polycrystalline was synthesized at 1500 °C in a muffle furnace by solid-state reaction method. A Φ 6 $\times$100 mm feed rod can be obtained after cold isostatic pressing and sintering.

The laser floating zone method was used for $TbInO_3$ crystal growth. The feed rod and seed rod were aligned in a coaxial line for crystal growth, and counter-rotation was adopted to improve the homogeneity of the melt zone.

2.2. Characterization

Single crystal X-ray diffraction data were collected with a Bruker SMART APEX-II diffractometer. Data integration and global unit cell refinements were carried out by the INTEGRATE program of APEX2-2014 software [39]. Absorption corrections were done by the SCALE program. The structure was solved and refined by the SHELXTL crystallographic software package. Anisotropic thermal parameters of all atoms were also refined and converged to $I > 2\sigma(I)$. The powder X-ray diffraction data were collected using a Panalytical X'Pert^3 diffractometer at room temperature (Cu Kα radiation). Data was collected in the scanning range of 10−100° with a step size of 0.01° and a scanning speed of 0.4 s/step. The crystallinity of the $TbInO_3$ crystal was evaluated by a real-time back-reflection Laue camera system (FDS Laue camera with PSL software). PL and PLE spectra of the $TbInO_3$ crystal were recorded by a fluorescence spectrometer (OmniFluo990LSP-M, Zolix, Beijing, China). Raman spectrum was obtained in a back-scattering configuration by a LabRAM HR Evolution system from Horiba Jobin Yvon at room temperature, and a 633 nm laser was used as the excitation source.

A piece of cleaved *ab* plane of $TbInO_3$ crystal was etched chemically in phosphoric acid at 180 °C for 30 min. The sample was then rinsed with clean water, and the domain patterns were observed under a Zeiss optical microscope. The Premier II Ferroelectric Test system (Radiant Technologies, Inc., Albuquerque, NM, USA) was employed to measure the electric polarization hysteresis loop and the positive-up-negative-down (PUND) method was adopted to get rid of leakage current and capacitance contribution [40–42].

3. Results and Discussion

3.1. Crystal Growth

In order to prevent the volatilization of indium element from the melt, the growth atmosphere and pressure were studied. Generally, the higher the growing atmosphere pressure, the more effective suppression of the volatilization of components. The maximum pressure of the growing atmosphere provided by the laser floating zone furnace is 10 MPa. Therefore, 9.5 MPa air, oxygen, argon, and nitrogen were respectively tried as growing atmosphere. The results showed that 9.5 MPa oxygen at a flow rate of 0.1 L/min was optimal for inhibiting the volatilization of indium.

Meanwhile, a faster growth rate is necessary to reduce the volatilization of indium. Different crystal growth rates were tried under an oxygen atmosphere of 9.5 MPa. When the crystal growth rate exceeded 20 mm/h, the crystal appeared to have poor crystalline quality and to crack. Crystal cracking is mainly caused by excessive growth rate and temperature gradient. When the crystal growth rate was slow (1–5 mm/h), volatilization of indium was quite serious in the crystal growth process. The optimal growth speed was determined as 12 mm/h.

Corresponding compensation for In_2O_3 should be considered due to the serious volatilization of indium during the crystal growth process. The $TbInO_3$ crystals were grown with extra In_2O_3 of 15 at.%, 10 at.%, and 5 at.% respectively. The crystallinity of crystal grown with an extra 5 at.% In_2O_3 was pretty poor. The second phase of In_2O_3 was observed in the $TbInO_3$ crystal when the amount of In_2O_3 exceeded the stoichiometric ratio of 15 at.%, and the pure phase of $TbInO_3$ crystal was obtained when the amount of In_2O_3 exceeded the stoichiometric ratio of 10 at.%, as shown in Figure 1. Therefore, an excess of 10.0 at.% of In_2O_3 is the suitable ratio and the $TbInO_3$ crystal grown with this ratio is shown in Figure 2.

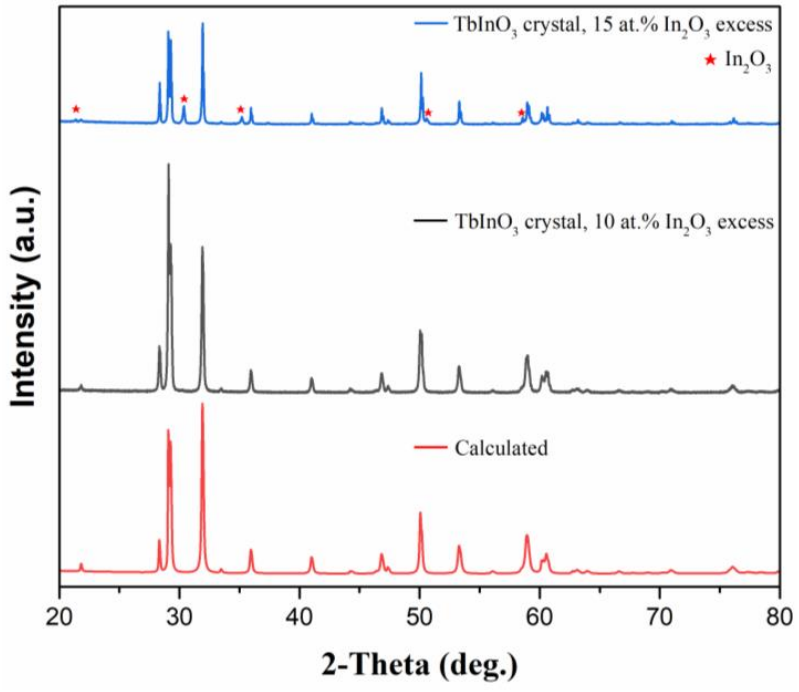

Figure 1. XRD of $TbInO_3$ crystals.

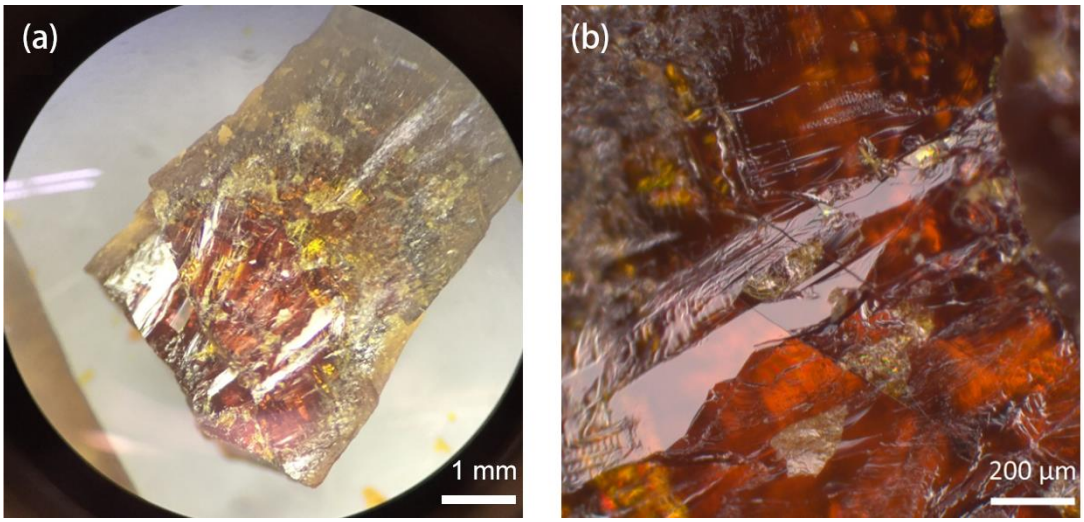

Figure 2. (**a**) Photograph of as-grown boule of $TbInO_3$. (**b**) The cleaved surface of $TbInO_3$ crystal.

3.2. Crystal Structure and Laue Measurements

Resolved crystal data and structure refinement of $TbInO_3$ are summarized in Table 1. $TbInO_3$ crystallizes in the hexagonal space group $P6_3cm$ with cell parameters a = 6.3088 (1) Å, c = 12.3067 (4) Å, and Z = 6. The atomic coordinates, isotropic thermal parameters, selected bond distances (Å) and angles (°) are listed in Tables S1 and S2 (Supporting Information). Further details of the crystal structure can be obtained from the Cambridge Crystallographic Data Centre (CCDC) using the depository number CSD 2234504. The Tb atoms were coordinated with seven O atoms, and the bond lengths ranged from 2.314 to 2.63 Å. The InO_5 bipyramids with the In–O bond distances varying between 2.077 and 2.143 Å.

Table 1. Crystal data and structure refinement for $TbInO_3$.

Formula	$TbInO_3$
FW (g·mol^{-1})	321.74
radiation wavelength	Mo Kα 0.71073 Å
crystal system	hexagonal
space group, Z	$P6_3cm$, 6
a (Å)	6.3088 (1) Å
c (Å)	12.3067 (4) Å
V (Å^3)	424.20 (2) Å^3
ρ_{calc} (g·cm^{-3})	7.557
absorp coeff (mm^{-1})	32.71
R(int)	0.081
GOF on F^2	1.257
R_1 ($I > 2\sigma_I$) [a]	0.0415
wR_2 ($I > 2\sigma_I$) [a]	0.0847
R_1 (all data) [a]	0.0449
wR_2 (all data) [a]	0.0885

[a] $R_1 = \sum ||F_o| - |F_c|| / \sum |F_o|$; $wR_2 = [\sum[w(F_o^2 - F_c^2)^2] / \sum[w(F_o^2)^2]]^{1/2}$, and $w = 1/[\sigma^2 F_o^2 + (A \cdot P)^2 + B \cdot P]$, $P = (F_o^2 + 2F_c^2)/3$; A and B are weight coefficients.

As shown in Figure 3a, InO_5 triangular bipyramids were separated by Tb^{3+} ions layers. The InO_5 bipyramids tilted, and the Tb^{3+} ions deviated from the mirror position, resulting in two unequal Wyckoff positions of *2a* and *4b* (Tb1 and Tb2). Along the c direction, Tb^{3+} ions presented up and down distortions, which caused ferroelectric polarization. This unusual driving mechanism has been referred to as "improper geometric ferroelectricity" [13,43]. As shown in Figure 3b,c, Tb^{3+} ions are arranged into a two-dimensional hexagonal structure in

each layer of the *ab* plane. The Tb2 sites form a honeycomb structure, and the Tb1 sites sit at the center of each honeycomb cell. Four identical Tb^{3+} ions form a parallelogram, and the distances between nearest-neighbor Tb^{3+} ions pairs were 3.67 Å (Tb1-Tb2) and 3.65 Å (Tb2-Tb2), respectively. This honeycomb structure supports the coexistence of ferroelectricity and a spin liquid state in $TbInO_3$.

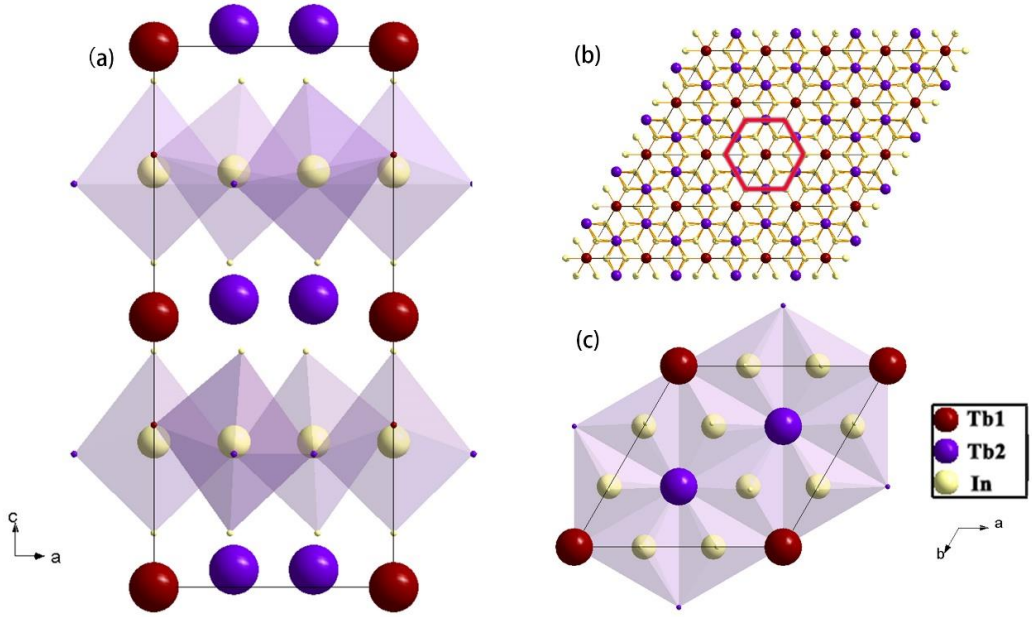

Figure 3. (**a**) Crystal structure of $TbInO_3$ in the [010] projection. Tb ions with two different sites (Tb1 and Tb2). (**b**) Tb^{3+} ions form a two-dimensional hexagonal lattice in the ab plane. (**c**) Nearest-neighbor Tb1-Tb2 and Tb2-Tb2 pairs.

Laue measurements were performed on $TbInO_3$ single crystal. As shown in Figure 4, the bright and clear diffraction spots on the *ab* plane of the crystal indicated the pure phase and hexagonal symmetry of the as-grown $TbInO_3$ crystal.

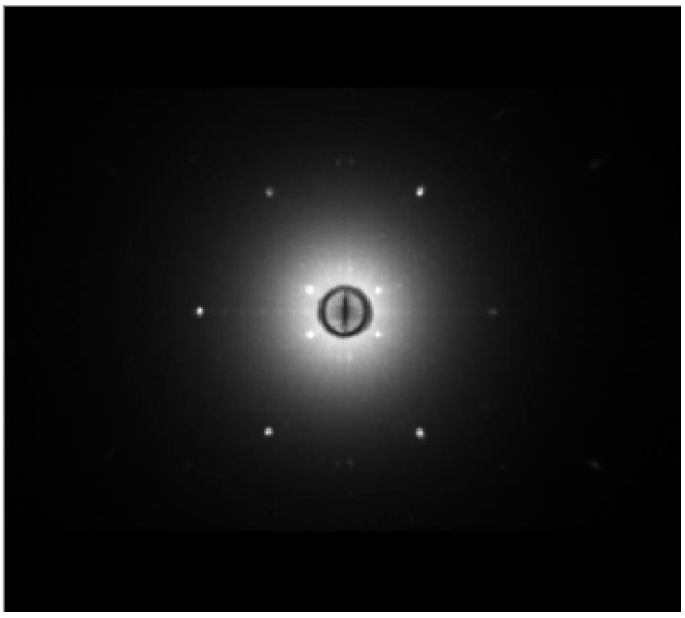

Figure 4. Laue patterns on *ab* plane of the $TbInO_3$ crystal.

3.3. PL and PLE Spectra

The PL and PLE spectra of the $TbInO_3$ crystal are displayed in Figure 5. From the PLE spectrum (λ_{em} = 547 nm), four excitation bands centered at 365, 413, 450, and 470 nm could be observed (Figure 5a), originating from the $^7F_6 \rightarrow {}^5D_3$, $^7F_5 \rightarrow {}^5D_3$, $^7F_3 \rightarrow {}^5D_3$, $^7F_6 \rightarrow {}^5D_4$ transitions of Tb^{3+} ion, respectively. The strongest excitation peak was located at 450 nm, matching the blue LD chips. By exciting $TbInO_3$ crystal under 450 nm, the emission peaks located at 547, 592, 623, and 648 nm were found in its PL spectra (Figure 5b), corresponding to the $^5D_4 \rightarrow {}^7F_J$ (J = 5, 4, 3, 2) transitions of Tb^{3+} ion, respectively. Among them, the emission peaks centered at 592 and 623 nm overlapped and formed an intensive broad emission band covering the yellow and orange regions.

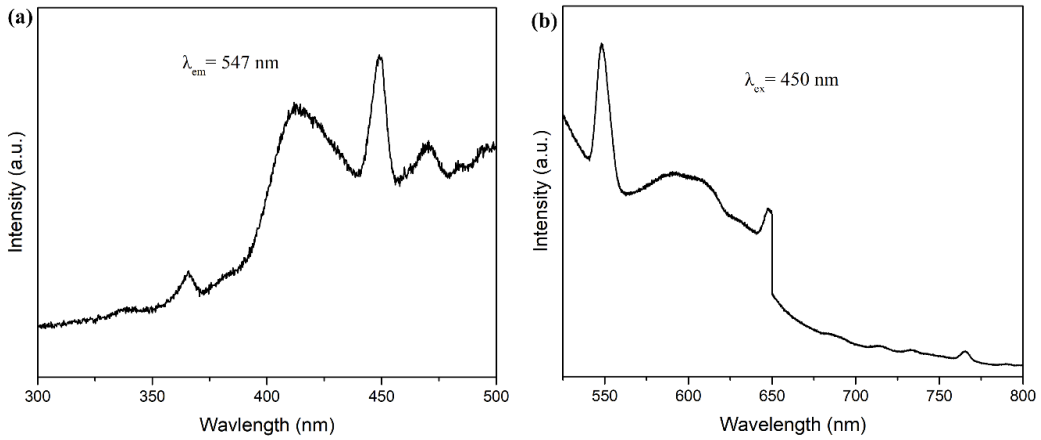

Figure 5. (**a**) Normalized PLE spectrum (λ_{em} = 547 nm). (**b**) Normalized PL spectrum (λ_{ex} = 450 nm).

3.4. Raman Spectrum

The measured Raman spectrum of the $TbInO_3$ crystal is plotted in Figure 6. The observed prominent Raman lines and low level of background proved the good quality of the as-grown crystal [44]. According to the simple harmonic oscillator approximation, the motion relevant to heavy ions should have appeared at the low-frequency region [45]. Tb^{3+} ion is the heaviest in the unit cell, and the low wavenumber modes at 64 cm^{-1} and 77 cm^{-1} are attributed to the vibrations of Tb^{3+} ions perpendicular and parallel to the *c*-axis, respectively. The strongest Raman mode at ~77 cm^{-1} is attributed to the vibration of Tb^{3+} ions along the c direction, corresponding to the generation of ferroelectric polarization. The mode at ~326 cm^{-1} was assigned as the A_{1g} symmetry, involving vibrations of O3(+*z*) − O4(−*z*) and O2(+*x*,*y*) − O1(−*x*,*y*). The Raman mode at ~362 cm^{-1} and 375 cm^{-1} belonged to the same E_{1g} symmetry, involving the vibration of oxygen ions in the *ab* plane. These two modes were partially overlapped and resembled coupled quantum oscillators. The mode at ~421 cm^{-1} was related to the bending vibration of InO_5 polyhedra, assigned as the A_{1g} symmetry. The Raman mode at ~605 cm^{-1} originated from the O1(+z) − O2(−z) vibration of InO_5 polyhedra. The InO_5 polyhedra were compressed by the repulsion between the electron density of Tb^{3+} 4f electrons and that of apical oxygen anions, which influenced the phonon dynamics of the $TbInO_3$ crystal structure.

3.5. Ferroelectric Properties

The interesting domain patterns on a surface of a chemically etched $TbInO_3$ crystal were observed using optical microscopy (Carl Zeiss Microscopy GmbH, Göttingen, Germany), as shown in Figure 7a. The two rather yellow regions were damaged pits that were generated during the cleavage process and are likely the defect sites on the surface. The domains with a size of 4~5 μm appeared as cloverleaf patterns, three of which were incident on each vertex. The link between vertices formed the pairing of vortices and antivortices, which could be analyzed by the graph theory [46]. The vortices display topological features with $Z_2 \times Z_3$ symmetry. Physically, Z_3 is assigned to three structural antiphase domains,

and Z_2 corresponds to the ferroelectric + and − domains. This type of topological domain indicated the improper ferroelectricity of the $TbInO_3$ crystal and supported the unique coupling between the ferroelectric and magnetic domain walls.

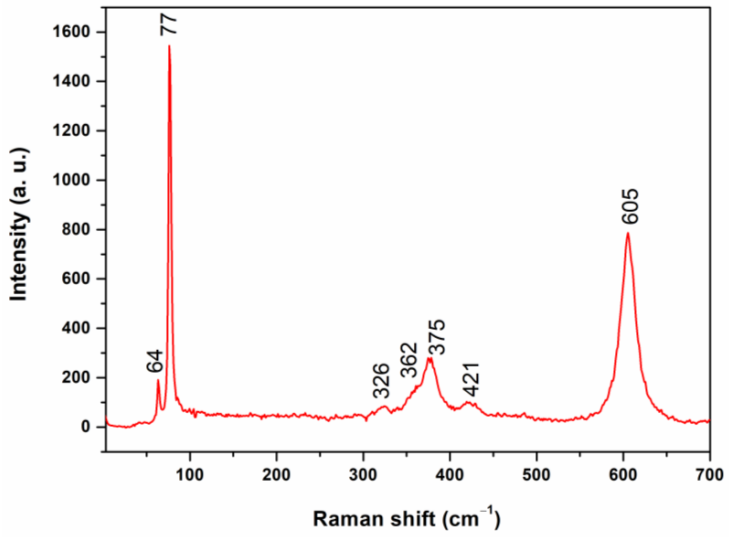

Figure 6. Raman spectrum of $TbInO_3$ crystal at room temperature.

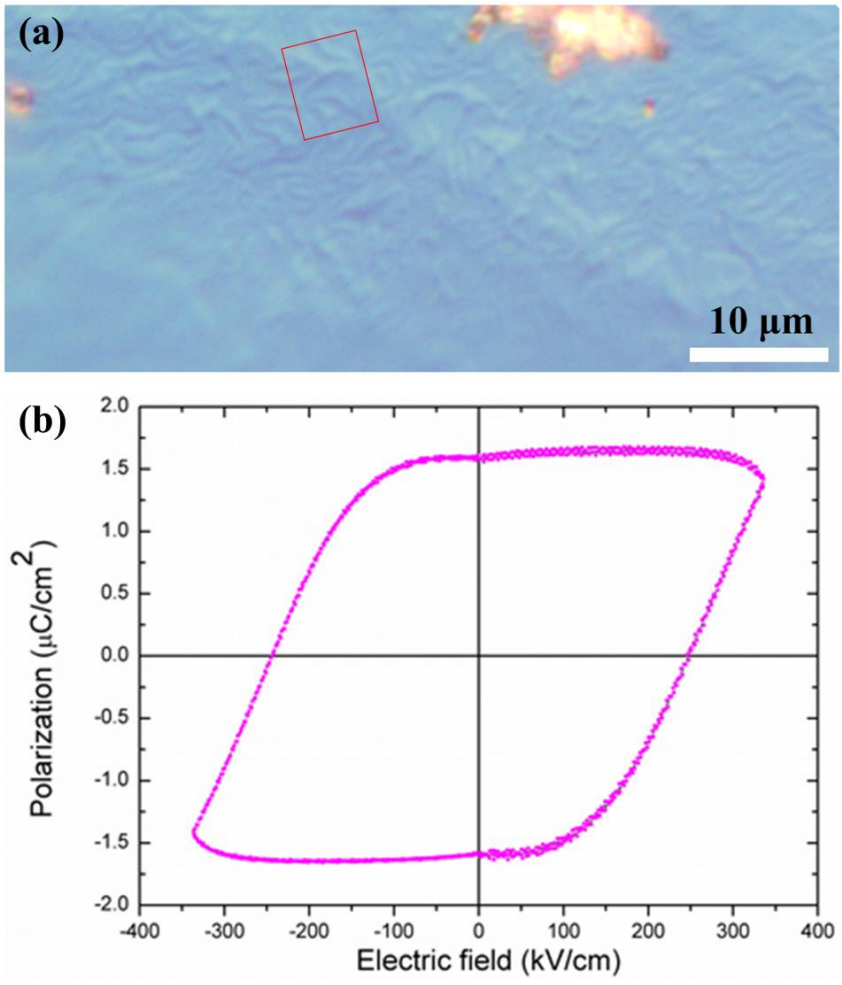

Figure 7. (**a**) Optical microscope image of chemically etched $TbInO_3$ crystal surface. (**b**) Electric polarization (P) versus electric field (E) hysteresis loops at room temperature.

As shown in Figure 7b, the P-E hysteresis loop was measured at room temperature with the frequency of f = 166 Hz, which demonstrated the presence of switchable ferroelectric polarization. The saturated polarization and coercive field along the direction [001] were 1.68 μC/cm^2 and 247 kV/cm, respectively. This improper ferroelectricity was caused by the structural distortion that intrinsically allows for the strong coupling between charge and spin, which provided great potential for vortex memory devices.

4. Conclusions

$TbInO_3$ crystal was grown by the laser floating zone technique. The crystallographic data of $TbInO_3$ were determined by single crystal diffraction, and the improper geometric ferroelectricity was mainly caused by up and down distortions of Tb^{3+} ions along the *c* direction. The lattice dynamics related to structure distortion were uncovered by Raman active vibration modes. The strongest excitation peak was located at 450 nm, and the emission peaks located at 547, 592, 623 and 648 nm were found in PL spectra. The topological vortex domains with a size of 4~5 μm were observed. The P-E hysteresis loops with saturated polarization of 1.68 μC/cm^2 were measured by the PUND method and demonstrated the presence of ferroelectricity. Our experimental results indicate that $TbInO_3$ crystal is a promising material for magnetoelectronic applications.

Supplementary Materials: The following supporting information can be downloaded at: https://www.mdpi.com/article/10.3390/cryst13020287/s1, Table S1: Refined atomic coordinates and isotropic displacement parameters for $TbInO_3$; Table S2: Selected bond lengths (Å) and angles (deg.) of $TbInO_3$.

Author Contributions: Conceptualization, C.M. and Y.L.; data curation, Y.W. and T.Z.; formal analysis, C.M. and C.Z.; funding acquisition, Y.L.; investigation, C.M., Y.W. and X.L.; methodology, C.M. and Y.W.; project administration, Y.L. and L.Z.; validation, C.M. and Y.W.; writing—original draft, C.M. and Y.W.; writing—review & editing, Y.L., S.-W.C. and L.Z. All authors have read and agreed to the published version of the manuscript.

Funding: The authors acknowledge the generous financial support from National Natural Science Foundation of China (51902143), the Natural Science Foundation of the Jiangsu Higher Education Institutes of China (19KJB430018), National Key Research and Development Program of China (2021YFB3501700), Key Research and Development Project of Jiangsu Province (BE2019033, BE2021040), Natural Science foundation of Jiangsu Province (BK20221226), Postgraduate Research & Practice Innovation Program of Jiangsu Province (SJCX21_1136, SJCX22_1255), and the U.S. DOE (DE-FG02-07ER46382).

Institutional Review Board Statement: Not applicable.

Informed Consent Statement: Not applicable.

Data Availability Statement: Not applicable.

Conflicts of Interest: The authors declare no conflict of interest.

References

1. Stein, J.; Biesenkamp, S.; Cronert, T.; Frohlich, T.; Leist, J.; Schmalzl, K.; Komarek, A.C.; Braden, M. Combined Arrhenius-Merz Law Describing Domain Relaxation in Type-II Multiferroics. *Phys. Rev. Lett.* **2021**, *127*, 097601. [CrossRef] [PubMed]
2. Kim, J.; Wang, X.; Huang, F.T.; Wang, Y.; Fang, X.; Luo, X.; Li, Y.; Wu, M.; Mori, S.; Kwok, D.; et al. Spin Liquid State and Topological Structural Defects in Hexagonal $TbInO_3$. *Phys. Rev. X* **2019**, *9*, 031005. [CrossRef]
3. Manz, S.; Matsubara, M.; Lottermoser, T.; Büchi, J.; Iyama, A.; Kimura, T.; Meier, D.; Fiebig, M. Reversible Optical Switching of Antiferromagnetism in $TbMnO_3$. *Nat. Photonics* **2016**, *10*, 653–656. [CrossRef]
4. Fiebig, M.; Lottermoser, T.; Meier, D.; Trassin, M. The Evolution of Multiferroics. *Nat. Rev. Mater.* **2016**, *1*, 16046. [CrossRef]
5. Lilienblum, M.; Lottermoser, T.; Manz, S.; Selbach, S.M.; Cano, A.; Fiebig, M. Ferroelectricity in the Multiferroic Hexagonal manganites. *Nat. Phys.* **2015**, *11*, 1070–1073. [CrossRef]
6. Bednorz, J.G.; Müller, K.A. Perovskite-Type Oxides—The New Approach to High-Tcsuperconductivity. *Rev. Mod. Phys.* **1988**, *60*, 585–600. [CrossRef]
7. Moritomo, Y.; Asamitsu, A.; Kuwahara, H.; Tokura, Y. Giant Magnetoresistance of Manganese Oxides with a Layered Perovskite Structure. *Nature* **1996**, *380*, 141–144. [CrossRef]
8. Cohen, R.E. Origin of Ferroelectricity in Perovskite Oxides. *Nature* **1992**, *358*, 136–138. [CrossRef]

9. Cheong, S.-W.; Mostovoy, M. Multiferroics a Magnetic Twist for Ferroelectricity. *Nat. Mater.* **2007**, *6*, 13–20. [CrossRef]
10. Zhang, Y.; Shimada, T.; Kitamura, T.; Wang, J. Ferroelectricity in Ruddlesden-Popper Chalcogenide Perovskites for Photovoltaic Application: The Role of Tolerance Factor. *J. Phys. Chem. Lett.* **2017**, *8*, 5834–5839. [CrossRef]
11. Panwar, N.; Singh, K.; Kanwar, K.; Bitla, Y.; Kumar, S.; Puli, V.S. Low-Temperature Magnetic and Magnetocaloric Properties of Manganese-Substituted $Gd_{0.5}Er_{0.5}CrO_3$ Orthochromites. *Crystals* **2022**, *12*, 263. [CrossRef]
12. Grover, V.; Shukla, R.; Jain, D.; Deshpande, S.K.; Arya, A.; Pillai, C.G.S.; Tyagi, A.K. Complex $GdSc_{1-x}In_xO_3$ Oxides: Synthesis and Structure Driven Tunable Electrical Properties. *Chem. Mater.* **2012**, *24*, 2186–2196. [CrossRef]
13. Van Aken, B.B.; Palstra, T.T.; Filippetti, A.; Spaldin, N.A. The Origin of Ferroelectricity in Magnetoelectric $YMnO_3$. *Nat. Mater.* **2004**, *3*, 164–170. [CrossRef]
14. Katsufuji, T.; Masaki, M.; Machida, A.; Moritomo, M.; Kato, K.; Nishibori, E.; Takata, M.; Sakata, M.; Ohoyama, K.; Kitazawa, K.; et al. Crystal Structure and Magnetic Properties of Hexagonal $RMnO_3$ (R = Y, Lu, and Sc) and the Effect of Doping. *Phys. Rev. B* **2002**, *66*, 134434. [CrossRef]
15. Li, J.; Sleight, A.W.; Subramanian, M.A. Determination of the Local Environment of Mn^{3+} and In^{3+} in the $YInO_3$–$YMnO_3$ Solid Solution, Which Exhibits an Intense Blue Color. *Chem. Mater.* **2016**, *28*, 6050–6053. [CrossRef]
16. Kim, M.G.; Winn, B.; Chi, S.; Savici, A.T.; Rodriguez-Rivera, J.A.; Chen, W.C.; Xu, X.; Li, Y.; Kim, J.W.; Cheong, S.W.; et al. Spin-Liquid-Like State in Pure and Mn-Doped $TbInO_3$ with a Nearly Triangular Lattice. *Phys. Rev. B* **2019**, *100*, 024405. [CrossRef]
17. Clark, L.; Sala, G.; Maharaj, D.D.; Stone, M.B.; Knight, K.S.; Telling, M.T.; Wang, X.; Xu, X.; Kim, J.; Li, Y.; et al. Two-Dimensional Spin Liquid Behaviour in the Triangular-Honeycomb Antiferromagnet $TbInO_3$. *Nat. Phys.* **2019**, *15*, 262–268. [CrossRef]
18. Fan, F.; Gao, Z.; Ponet, L.; Wang, J.; Huang, H.; Artyukhin, S.; Hong, J.; Cheong, S.-W.; Wang, X. Visualization of Large-Scale Charged Domain Walls in Hexagonal Manganites. *Appl. Phys. Lett.* **2021**, *118*, 072901. [CrossRef]
19. Wang, X.; Yang, D.; Zhang, H.-M.; Song, C.; Wang, J.; Tan, G.; Zheng, R.; Dong, S.; Cheong, S.-W.; Zhang, J. Anisotropic Resistance Switching in Hexagonal Manganites. *Phys. Rev. B* **2019**, *99*, 054106. [CrossRef]
20. Lin, S.-Z.; Wang, X.; Kamiya, Y.; Chern, G.-W.; Fan, F.; Fan, D.; Casas, B.; Liu, Y.; Kiryukhin, V.; Zurek, W.H.; et al. Topological Defects as Relics of Emergent Continuous Symmetry and Higgs Condensation of disorder in Ferroelectrics. *Nat. Phys.* **2014**, *10*, 970–977. [CrossRef]
21. Geng, Y.; Das, H.; Wysocki, A.L.; Wang, X.; Cheong, S.W.; Mostovoy, M.; Fennie, C.J.; Wu, W. Direct Visualization of Magnetoelectric Domains. *Nat. Mater.* **2014**, *13*, 163–167. [CrossRef] [PubMed]
22. Cichy, K.; Świerczek, K. Influence of Doping on the Transport Properties of $Y_{1-x}In_xMnO_{3+\Delta}$ (Ln: Pr, Nd). *Crystals* **2021**, *11*, 510. [CrossRef]
23. Dong, C.; Chen, R.; Liu, Y.; Liu, C.; Zhu, H.; Ke, J.; Liu, W.; Yang, M.; Wang, J. Field-Induced Magnetic Phase Transitions and Rich Phase Diagram of $HoMnO_3$ Single Crystal. *Crystals* **2019**, *9*, 419. [CrossRef]
24. Balli, M.; Roberge, B.; Fournier, P.; Jandl, S. Review of the Magnetocaloric Effect in $RMnO_3$ and RMn_2O_5 Multiferroic Crystals. *Crystals* **2017**, *7*, 44. [CrossRef]
25. Yin, X.; Li, Y.; Wang, G.; Hu, J.; Xu, C.; Lu, Q.; Zhong, Y.; Zhao, J.; Zhao, X.; Zhang, Y.; et al. Magnetic Properties of the Quasi Two-Dimensional Centered Honeycomb Antiferromagnet $GdInO_3$. *Phys. Rev. B* **2021**, *104*, 134432. [CrossRef]
26. Kaiwart, R.; Dwivedi, A.; Shukla, R.; Velaga, S.; Grover, V.; Poswal, H.K. High Pressure Structural Evolution of Cubic Solid Solution $YbInO_3$. *J. Appl. Phys.* **2021**, *130*, 035902. [CrossRef]
27. Hartley, P.; Egdell, R.G.; Zhang, K.H.L.; Hohmann, M.V.; Piper, L.F.J.; Morgan, D.J.; Scanlon, D.O.; Williamson, B.A.D.; Regoutz, A. Experimental and Theoretical Study of the Electronic Structures of Lanthanide Indium Perovskites $LnInO_3$. *J. Phys. Chem. C Nanomater. Interfaces* **2021**, *125*, 6387–6400. [CrossRef]
28. Yu, Y.; Lin, N.; Wang, H.; Xu, R.; Ren, H.; Zhao, X. First Principles Study of Ferroelectric Hexagonal Compounds $RInO_3$ (R = Dy, Er, and Ho): Electronic Structure, Optical and Dielectric Properties. *RSC Adv.* **2020**, *10*, 4080–4086. [CrossRef]
29. Romanov, A.N.; Haula, E.V.; Shashkin, D.P.; Korchak, V.N. Broadband near-Ir Photoluminescence of Trigonal-Bipyramidal Coordinated Cu^{2+} Impurity Center in $YGaO_3$, $YInO_3$ and $GdInO_3$ Hexagonal Phases. *J. Lumin.* **2020**, *228*, 117652. [CrossRef]
30. Öztürk, E.; Karacaoglu, E. The Effect of Eu^{3+}-Doping on the Photoluminescent Properties of $ReInO_3$ (Re = Er, Sm) Type Phosphors. *Mater. Today Commun.* **2020**, *25*, 101556. [CrossRef]
31. Ye, M.; Kung, H.H.; Rosa, P.F.S.; Rosenberg, E.; Kim, J.; Xu, X.H.; Bauer, E.D.; Fisk, Z.; Fisher, I.R.; Cheong, S.W.; et al. Crystal-Field Excitations and Quadrupolar Fluctuations of 4f-Electron Systems Studied by Polarized Light Scattering. *J. Phys. Conf. Ser.* **2022**, *2164*, 012054. [CrossRef]
32. Tohei, T.; Moriwake, H.; Murata, H.; Kuwabara, A.; Hashimoto, R.; Yamamoto, T.; Tanaka, I. Geometric Ferroelectricity in Rare-Earth Compounds $RGaO_3$ and $RInO_3$. *Phys. Rev. B* **2009**, *79*, 144125. [CrossRef]
33. Shukla, R.; Grover, V.; Deshpande, S.K.; Jain, D.; Tyagi, A.K. Synthesis and Structural and Electrical Investigations of a Hexagonal $Y_{1-X}Gd_XInO_3$ ($0.0 \leq x \leq 1.0$) System Obtained Via Metastable C-Type Intermediates. *Inorg. Chem.* **2013**, *52*, 13179–13187. [CrossRef]
34. Shukla, R.; Sayed, F.N.; Grover, V.; Deshpande, S.K.; Guleria, A.; Tyagi, A.K. Quest for Lead Free Relaxors in $YIn_{1-X}Fe_XO_3$ ($0.0 \leq x \leq 1.0$) System: Role of Synthesis and Structure. *Inorg. Chem.* **2014**, *53*, 10101–10111. [CrossRef]
35. Shukla, R.; Grover, V.; Srinivasu, K.; Paul, B.; Roy, A.; Gupta, R.; Tyagi, A.K. Rare Earth Indates (Re: La–Yb): Influence of the Synthesis Route and Heat Treatment on the Crystal Structure. *Dalton Trans.* **2018**, *47*, 6787–6799. [CrossRef]

36. Li, Y.; Wang, Y.; Tan, W.; Wang, W.; Zhang, J.; Kim, J.W.; Cheong, S.-W.; Tao, X. Laser Floating Zone Growth of Improper Geometric Ferroelectric $GdInO_3$ Single Crystals with Z_6 Topological Defects. *J. Mater. Chem. C* **2018**, *6*, 7024–7029. [CrossRef]
37. Wu, Y.; Li, Y.; Zhou, C.; Chen, H.; Cheong, S.-W.; Li, Y.; Tao, X.; Zhang, L. Novel Geometric Ferroelectric $EuInO_3$ Single Crystals with Topological Vortex Domains. *Cryst. Growth Des.* **2023**. [CrossRef]
38. Savary, L.; Balents, L. Quantum Spin Liquids: A Review. *Rep. Prog. Phys.* **2017**, *80*, 016502. [CrossRef]
39. Zhang, J.; Zhang, Z.; Zhang, W.; Zheng, Q.; Sun, Y.; Zhang, C.; Tao, X. Polymorphism of $BaTeMo_2O_9$: A New Polar Polymorph and the Phase Transformation. *Chem. Mater.* **2011**, *23*, 3752–3761. [CrossRef]
40. Chai, Y.S.; Oh, Y.S.; Wang, L.J.; Manivannan, N.; Feng, S.M.; Yang, Y.S.; Yan, L.Q.; Jin, C.Q.; Kim, K.H. Intrinsic Ferroelectric Polarization of Orthorhombic Manganites Withe-Type Spin Order. *Phys. Rev. B* **2012**, *85*, 184406.
41. Feng, S.M.; Chai, Y.S.; Zhu, J.L.; Manivannan, N.; Oh, Y.S.; Wang, L.J.; Yang, Y.S.; Jin, C.Q.; Kim, K.H. Determination of the Intrinsic Ferroelectric Polarization in Orthorhombic $HoMnO_3$. *New J. Phys.* **2010**, *12*, 073006. [CrossRef]
42. Scott, J.F.; Kammerdiner, L.; Parris, M.; Traynor, S.; Ottenbacher, V.; Shawabkeh, A.; Oliver, W. Switching Kinetics of Lead Zirconate Titanate Submicron Thin-Film Memories. *J. Appl. Phys.* **1988**, *64*, 787–792. [CrossRef]
43. Ederer, C.; Spaldin, N.A. A New Route to Magnetic Ferroelectrics. *Nat. Mater.* **2004**, *3*, 849–851. [CrossRef] [PubMed]
44. Zhao, S.; Yu, T.; Wang, Z.; Wang, S.; Wei, L.; Chen, X.; Wang, S. Flux Method Growth of Large Size Group IV–V 2d Gep Single Crystals and Photoresponse Application. *Crystals* **2021**, *11*, 235. [CrossRef]
45. Paul, B.; Chatterjee, S.; Gop, S.; Roy, A.; Grover, V.; Shukla, R.; Tyagi, A.K. Evolution of Lattice Dynamics in Ferroelectric Hexagonal $ReInO_3$ (Re = Ho, Dy, Tb, Gd, Eu, Sm) Perovskites. *Mater. Res. Express* **2016**, *3*, 075703. [CrossRef]
46. Chae, S.C.; Horibe, Y.; Jeong, D.Y.; Rodan, S.; Lee, N.; Cheong, S.W. Self-Organization, Condensation, and Annihilation of Topological Vortices and Antivortices in a Multiferroic. *Proc. Natl. Acad. Sci. USA* **2010**, *107*, 21366–21370. [CrossRef]

Disclaimer/Publisher's Note: The statements, opinions and data contained in all publications are solely those of the individual author(s) and contributor(s) and not of MDPI and/or the editor(s). MDPI and/or the editor(s) disclaim responsibility for any injury to people or property resulting from any ideas, methods, instructions or products referred to in the content.